A topographic drag closure built on an analytical base flux

by

Stephen T. Garner
Geophysical Fluid Dynamics Laboratory/NOAA
Princeton NJ

Author address:

GFDL/NOAA
P.O. Box 308
Princeton University
Princeton, NJ 08542

steve.garner@noaa.gov

Abstract

Topographic drag schemes depend on grid-scale representations of the average height, width and orientation of the subgrid topography. Until now, these representations have been based on a combination of statistics and dimensional analysis. However, under certain physical assumptions, linear analysis provides the exact amplitude and direction of the drag over arbitrary topography. The author proposes a computationally practical closure built on this analysis, along with a nonlinear extension. The extension to nonlinear flow is based on traditional dimensional reasoning but achieves a better match with the linear drag by exploiting the correlation between mountain height and width.

The nonlinear extension is also used, with standard assumptions about the wavebreaking process, to quantify the transition to saturation in the wavetrain. This yields the vertical distribution of the momentum forcing and completes the scheme. The explicit subgrid height distribution causes a natural broadening of the layers subjected to forcing.

Linear drag due to simple oscillating flow over topography, which is relevant to ocean tides, has almost the same form as for the stationary atmospheric problem. However, the dimensional analysis suggests that the nonlinear drag is mostly due to topographic length scales that are small enough to keep the steady-state assumption well satisfied.

1. Introduction

Mountain drag parameterizations estimate the transfer of momentum across the topographic boundary (the “base flux”) as well as the convergence of the pseudomomentum flux as a function of height above the boundary. Previous schemes for estimating the base flux have relied entirely on statistical measures of the height, shape and orientation of the unresolved terrain, guided by dimensional reasoning (e.g., Baines and Palmer 1990, Bacmeister 1993, Lott and Miller 1997, Scinocca and McFarlane 2000). Here we propose a scheme that uses an analytical estimate of the drag vector. This estimate is exact in the limit in which the mountain waves are linear, inviscid and hydrostatic, and the medium is nonrotating and uniform in time and space.

We also propose a correction for nonlinearity at the source. This is similar in many ways to existing schemes that allow a gradual transition between linear and nonlinear dimensional drag laws (e.g., Kim and Arakawa, 1995, and references therein; Lott and Miller, 1997; Scinocca and McFarlane, 2000). However, the proposed treatment exploits the correlation of mountain height with mountain width together with the known range of heights within the gridcell. The motivation for adding complexity here is to obtain a closer match to the analytical result in the linear limit as well as a less arbitrary transition to nonlinearity. A beneficial side-effect is to make the overall scheme less “tunable”.

The impact of the subgrid topography on the resolved flow is due to the convergence of the pseudomomentum flux. A straightforward extension of the nonlinear base-flux correction yields an algorithm for clipping the flux to the saturation value as a function of height in order to determine the forcing of the resolved flow. This part of the scheme adheres to traditional assumptions going back to Lindzen (1981), Palmer *et al*. (1986) and Pierrehumbert (1987).

2. Base-flux closure

Drag parameterizations for the atmosphere generally assume that the disturbance is steady and contains only upward-propagating waves. If we add to these assumptions certain constraints on the horizontal scale of the forcing, such that the waves are broad enough to be hydrostatic but narrow enough to be unaffected by sphericity, rotation, horizontal shear or baroclinicity, we can calculate the total drag in the linear limit as accurately as we know the shape of the terrain. In this section, we begin with the linear analysis and then describe the proposed extension to nonlinear base flux.

2a. Linear drag

We suppose that the topography can be analyzed into Fourier amplitudes $\hat{h}(\boldsymbol{k})$, where $\boldsymbol{k} = (k, l)$ is the horizontal wavenumber. This is reasonable because the scales of interest are much smaller than the planetary scale. We write $\overline{V}_{\boldsymbol{k}} \equiv \overline{\boldsymbol{V}} \cdot \boldsymbol{k}/|\boldsymbol{k}|$ for the component of the resolved flow, $\overline{\boldsymbol{V}}$, parallel to $\boldsymbol{k}$. The linearized lower boundary condition is $w = \overline{\boldsymbol{V}} \cdot \nabla h$, or

$$\hat{W}(\boldsymbol{k}) = \overline{V}_{\boldsymbol{k}} i |\boldsymbol{k}| \hat{h}(\boldsymbol{k}), \tag{1}$$

where $\hat{W}$ is the transform of $W(x, y) \equiv w(x, y, z = 0)$, the vertical velocity component at the ground. With this transform, we have assumed that all other spatial variability in the flow has much larger horizontal scales than the mountain waves.

We assume gradual vertical variations such that $d|m|^{-1}/dz \ll 1$, where m is the stationary vertical wavenumber, and also assume $m \gg \bar{\rho}^{-1}|d\bar{\rho}/dz|$, where $\bar{\rho}(z)$ is the density profile. If we neglect horizontal variations of the buoyancy frequency, $\overline{N}$, and consider only hydrostatic scales $|\boldsymbol{k}| \ll |m|$, the WKB approximation for the vertical structure is

$$\hat{w}(\boldsymbol{k}, z) = \hat{W}(\boldsymbol{k}) \exp\left(i \int_0^z m\, dz'\right) \exp(z/2H), \tag{2}$$

with $H = \bar{\rho}/(-d\bar{\rho}/dz)$ and $m = \bar{N}/\bar{V}_{\boldsymbol{k}} + O(\lambda^2/H^2)$ (*e.g.*, Holton 1973). Here λ denotes a scale for the vertical wavelength, inversely proportional to the typical wavenumber m. It then follows from (1) and (2) that, at the surface,

$$\partial(\bar{\rho}\hat{w})/\partial z = -\bar{\rho}[\bar{N} + i\bar{V}_{\boldsymbol{k}}/(2H)]|\boldsymbol{k}|\hat{h} + O(\lambda^2/H^2)\,. \qquad (3)$$

Since there is no source of vertical vorticity at the ground, the horizontal velocity perturbation, say $\boldsymbol{V}'$, is completely determined by a scalar potential, $\chi(x, y)$, such that $\nabla\chi = \bar{\rho}\boldsymbol{V}'$ (here and in the following, ∇ denotes the horizontal operator). Mass conservation implies $\nabla^2\chi = -\partial(\bar{\rho}w)/\partial z$, which, with (3), leads to

$$\hat{\chi}(k, l) = -\bar{\rho}\bar{N}\frac{\hat{h}(\boldsymbol{k})}{|\boldsymbol{k}|} - \frac{\bar{\rho}}{2H}\frac{\hat{h}(\boldsymbol{k})}{|\boldsymbol{k}|^2}i\boldsymbol{k}\cdot\bar{\boldsymbol{V}}\,. \qquad (4)$$

Here we have retained only the $O(\lambda/H)$ correction, the term involving $\bar{\boldsymbol{V}}$, which we call $\hat{\chi}_1$. The dominant first term, say $\hat{\chi}_0$, does not depend on the resolved wind and produces

$$\chi_0(x, y) = -\bar{\rho}\bar{N}\iint\frac{\hat{h}(\boldsymbol{k})}{|\boldsymbol{k}|}\exp(i\boldsymbol{k}\cdot\boldsymbol{x})dkdl\,, \qquad (5)$$

with $\boldsymbol{x} = (x, y)$. Thus, χ_0 is a slightly smoothed transformation of the terrain height. The velocity perturbation $(1/\bar{\rho})\nabla\chi_0$ produced by each spectral component of $h(x, y)$ is perpendicular to the corresponding phase lines of the topography and directed downhill.

If the integral in (5) converges, the spatial-transform equivalent is

$$\boxed{\chi_0(x, y) = -\frac{\bar{\rho}\bar{N}}{2\pi}\iint\frac{h(\boldsymbol{x}')}{|\boldsymbol{x}-\boldsymbol{x}'|}dx'dy'.} \qquad (6)$$

The correction due to the vertical density gradient can also be put into the spatial domain. The easiest way is to define $A(x, y) = -\nabla^{-2}h$ so that $\chi_1 = -\frac{\bar{\rho}}{2H}\bar{\boldsymbol{V}}\cdot\nabla A$.

These integrals diverge if $\hat{h}$ does not decrease as fast as $|\boldsymbol{k}|$ for small $|\boldsymbol{k}|$ (large scales).

However, the result is already physically inconsistent at large scales. For both mathematical convergence and physical consistency, the input topography must be filtered to retain only the scales that force stationary, nonrotating gravity waves. Then, as a practical matter, (6) need not be integrated over the entire globe for each $\boldsymbol{x}$, but only over a radius equal to a small multiple of the high-pass filter scale. It is simplest to allow the topographic dataset to establish the low-pass scale. The problem of filtering has been discussed by most drag-scheme developers, including Baines and Palmer (1990), Lott and Miller (1997) and Scinocca and McFarlane (2000). We also say more about it just below.

Although $\boldsymbol{V}'$ has only a weak dependence on $\bar{\boldsymbol{V}}$, the momentum flux across a horizontal surface, namely,

$$\tau(x, y) = \bar{\rho} w \boldsymbol{V}', \tag{7}$$

depends strongly on the resolved wind because of the boundary condition $w = \bar{\boldsymbol{V}} \cdot \nabla h$. Let $\tilde{\chi} = (\rho_r N_r / \bar{\rho} \bar{N}) \chi$, where the subscript “r” denotes constant reference values. Then

$$\tau = \frac{\bar{\rho} \bar{N}}{\rho_r N_r} [\nabla \tilde{\chi} (\nabla h)^T] \bar{\boldsymbol{V}}, \tag{8}$$

and the outer product, $\nabla \tilde{\chi} (\nabla h)^T \equiv \mathbf{T}$, depends only on the terrain except for the small contribution to $\tilde{\chi}$ from χ_1. Subject to our assumptions, $\mathbf{T}$ contains all relevant information about the topography, including amplitude, variance, orientation and anisotropy. Using angle brackets to denote a gridcell average, we can write

$$\boxed{\langle \tau \rangle = \frac{\bar{\rho} \bar{N}}{\rho_r N_r} \langle \mathbf{T} \rangle \bar{\boldsymbol{V}}} \tag{9}$$

for the estimate of drag at a model grid-point. When χ_1 is included, the dependence on $\bar{\boldsymbol{V}}$ is partly quadratic but the coefficients still depend only on the terrain.

Because of the high-pass filtering, it should be consistent to regard (5) as an integral over spherical harmonics with $|\boldsymbol{k}|$ still denoting the total wavenumber. Spherical-harmonic analysis of h may also be a practical way to obtain the field $A(x, y)$ and the second partial derivatives of A needed for the $O(\lambda/H)$ correction to $\mathbf{T}$. For the examples to follow, we ignored this correction and obtained the flow disturbance from (6). We pre-processed the topography using a filter that passes only scales of less than about 1.5 deg of longitude and latitude in the extratropics. The filtering scale, d, was allowed to vary with latitude so as to keep the Rossby number, V/fd, of order unity, where $V(y)$ is a profile of typical surface wind speeds and $f(y)$ is the Coriolis parameter. The horizontal derivatives in (8) make the result fairly insensitive to the choice of scales retained by a high-pass filter, and this seems to allow a time-independent choice for $d(y)$.

The use of a physically based filter instead of one based on the grid size (or a combination of the two, as in Scinocca and McFarlane, 2000) makes it possible to double-count the drag when the grid spacing is smaller than d. This has to be avoided by defining the “subgrid drag” as the difference between the total parameterized drag and the model-dependent resolved drag. Then the subgrid contribution is not known until the resolved drag is diagnosed. In many climate-model applications, resolved drag can be neglected. This approach does not solve the problem of representing strong scale interactions near the grid scale. All closure schemes have this generic weakness (*e.g.*, consider any moist convection scheme in either the time or space domain). Unfortunately, it is not alleviated by using a grid-based filter.

From (6), the velocity scales as $N_r h'$, where h' is a measure of the mesoscale (drag-producing) component of the topographic height. Therefore, mountain-wave velocities have an order of magnitude of $V' \sim (10^{-2}\mathrm{s}^{-1})(10^{3}\mathrm{m}) = 10\mathrm{ms}^{-1}$, given a typical mesoscale relief of $h' \sim 1000\ \mathrm{m}$. If the scale of the topography is 100 km and the ambient wind is of order 10 ms^{-1}, the vertical velocity is of order 0.1 ms^{-1}. It follows that the drag is characteristically

$D \sim \rho_r(10\ \mathrm{ms}^{-1})(0.1\mathrm{ms}^{-1}) \sim 1\mathrm{Pa}$. The tensor $\mathbf{T}$ is dominated by the diagonal elements, which are of the order of $\rho_r(10\ \mathrm{ms}^{-1})$.

Shown in Fig. 1 is a plot of the linear drag $\langle\tau\rangle$ over the Western Hemisphere for an assumed large-scale wind that is purely zonal at -7 m/s in the tropics and 13 m/s in the extratropics. A constant surface buoyancy frequency, $\bar{N} = 0.01\mathrm{s}^{-1}$, and density, $\bar{\rho} = 1\ \mathrm{kg/m}^3$, are assumed. The same calculation for the Asian continent, shown in Fig. 2, assumes a large-scale wind from the west at 10 m/s everywhere. The averaging in both Fig. 1 and Fig. 2 is over latitude-longitude cells of about 1.5 deg on a side. The topography has a resolution of 1/30 degree.

2b. Nonlinear extension

Nonlinearity is measured by the nondimensional mountain height, $\tilde{h} = (\bar{N}/\bar{V})h$. We can write the lower boundary condition as a perturbation series based on $\tilde{h}$ (*e.g.*, Smith 1977):

$$w - \bar{\boldsymbol{V}} \cdot \nabla h = \boldsymbol{V}' \cdot \nabla h - \bar{\boldsymbol{V}} \cdot \nabla(\delta_z h) + h\bar{\boldsymbol{V}}_z \cdot \nabla h + \ldots, \tag{10}$$

where δ is the lowest-order vertical particle displacement (with δ_z its first derivative) and $\bar{\boldsymbol{V}}_z$ is the resolved vertical shear. The first-order nonlinearities are represented by the three explicit terms on the right-hand side. The first two are associated with low-level blocking (*e.g.*, Pierrehumbert and Wyman 1985), deflection (*e.g.*, Miranda and James 1992) and periodic steepening above the mountain (Smith 1977). Blocking and deflection alter the total drag and cause some of it -- the “nonpropagating” part -- to be deposited at low levels close to the source. The third term could be included analytically by replacing (9) with

$$\langle\tau\rangle = \frac{\bar{\rho}\bar{N}}{\rho_r N_r}(\langle\mathbf{T}\rangle\bar{\boldsymbol{V}} + \langle\mathbf{S}\rangle\bar{\boldsymbol{V}}_z), \tag{11}$$

where $\mathbf{S} = h\nabla\tilde{\chi}(\nabla h)^T$. However, this correction is less significant than the other two nonlinear effects when the local Richardson number, $\bar{N}^2/(\bar{\boldsymbol{V}}_z)^2$, is large. The Richardson number is assumed to be large in making the WKB approximation leading to (5). Moreover, the uncertainty about the proper value of $\bar{\boldsymbol{V}}$ (and $\bar{N}$) to use when a planetary mixed layer is present could easily exceed the size of a correction for $\bar{\boldsymbol{V}}_z$.

We will evaluate the nonpropagating drag due to blocking mountains by resorting to dimensional analysis and assuming a fast "orographic adjustment" process (Pierrehumbert and Wyman 1985, Pierrehumbert 1987, Olaffson and Bougeault 1996). What follows is a fairly standard treatment along these lines (*e.g.*, Lott and Miller 1997), except that we will allow for a range of mountain heights within the gridcell. As mentioned briefly at the beginning, the motivation for adding complexity here is (1) to produce a better match between the linear solution and the dimensional estimate in the limit of small terrain and (2) to set up a more rational, less tunable, transition to partially blocked flow. Thus, the analytical result will be used to constrain the drag coefficient for propagating components, and this scaling, together with some assumptions about the mountain *ensemble* within the gridcell, will determine the transition to partially blocked flow. Since the "excess" mountain height responsible for blocking cannot be straightforwardly attributed to spectral components, two key assumptions will be (1) that the topography is characterized by well-defined features, each with a well-defined areal extent, that can be binned into height ranges, and (2) that the flow disturbances induced by these features do not interact strongly.

i. Drag model for individual features

If the mountain height exceeds a certain threshold, h_c, that depends on both $\bar{V}$ and $\bar{N}$, the flow is blocked or deflected below the level $z = h - h_c$. Here we are thinking of h as the height of an individual mountain rather than a continuous distribution in space. For mountains with heights less than h_c, the drag is entirely linear and propagating. For those greater than h_c, it includes a propagating and a nonpropagating contribution, as shown schematically in Fig. 3. The part that launches internal waves has a height of h_c, measuring down from the summit. In order

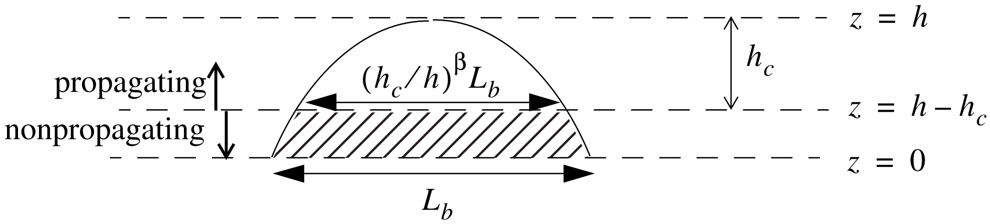

Fig. 3

to relate the width L of this part of the mountain to elevation above the base, a power law with parameter β is introduced:

$$L(z) = L_b(1 - z/h)^{\beta}. \tag{12}$$

Thus, $\beta = 1$ corresponds to triangular mountains, $\beta < 1$ to blunt mountains and $\beta > 1$ to pointed ones. This shape is a generalization of the one assumed by Lott and Miller (1997), which corresponds to $\beta = 0.5$.

The linear drag law is $D_l \sim \rho N V h^2 / L$, where V and L are the ambient wind component and the width of the mountain, respectively, measured in the same direction. As the flow becomes blocked by topography, the drag law in the blocked layer changes to $D_{nl} \sim \rho V^2 (h - h_c)/L$. Orographic adjustment essentially means that the nondimensional depth $\tilde{h} = h(N/V)$ of the (marginally) laminar flow below the summit is set by a universal threshold, $\tilde{h}_c = h_c(N/V)$, related to the critical Froude number. For a meaningful Froude number, V should be the wind component opposite the drag, which is an average of $\mathbf{V}'$ weighted by the mountain slope in the ambient wind direction. The assumption that the blocked flow adjusts to the depth $z = h - h_c$ independently for each feature with no downstream interference may be the weakest part of this closure.

To account for the tapering of the mountain, we slightly refine the formula for the nonlinear drag per unit area as $D_{nl} \sim \rho V^2 \int L(z) dz / L_b^2$, with the integral ranging from zero to $h - h_c$

(see the hatched cross-section in Fig. 3). Then the total drag per unit area exerted by a mountain is sum of the two components,

$$\begin{aligned} D_p &= a_0 \min\{1, (\tilde{h}_c/\tilde{h})^{2-\beta}\}\tilde{h}^2(\bar{\rho}\bar{V}^3/\bar{N}L_b), \\ D_{np} &= a_1(1-\min\{1, (\tilde{h}_c/\tilde{h})^{1+\beta}\})\frac{\tilde{h}}{1+\beta}(\bar{\rho}\bar{V}^3/\bar{N}L_b)\ , \end{aligned} \tag{13}$$

where D_p and D_{np} denote the propagating and nonpropagating parts of the base flux, respectively, and a_0 and a_1 are constant drag coefficients. This purely dimensional formulation is similar to that of Lott and Miller (1997) but it limits the propagating drag to the saturation value when $\tilde{h} > \tilde{h}_c$ and does not assume $\beta = 1/2$. The parameter β appears in D_p because the propagating drag is inversely proportional to L. It appears in D_{np} because of the tapering of the mountain cross-section.

ii. Drag model for the gridcell ensemble

Drag closures typically take L_b in (13) to be a universal constant and equate $\tilde{h}^2$ to the mean-squared height of the filtered topography within the gridcell. However, it should be easier to match the analytical drag if h and L_b are allowed to co-vary when averaging (13) over the gridcell. In the general case with both $D_{np} \neq 0$ and $D_p \neq 0$ it is impractical to average over the explicit subgrid height distribution because, while $\tilde{h}_c$ is assumed constant, $\tilde{h}$ is time-dependent.

We consider a particularly simple relationship between h and L_b that keeps the overall computation tractable. The analysis in the appendix suggests that we may assume a power law,

$$L/L_0 = (h/h_0)^\gamma, \tag{14}$$

where L_0, h_0 and γ are universal constants and L refers to L_b. Our best global estimate is around $\gamma = 0.4$. Although the relation (14) seems to suggest a $-2/\gamma$ power spectrum for topographic height, it is actually a probability distribution across height bins rather than spectral components. The functional form of (14) satisfies the reasonable requirement of monotonicity and the practical requirement of integrability in closed form.

If we can neglect overlaps between mountains and ignore any correlation between anisotropy and mountain height, the areal coverage $dA \sim LdL$ of features in the range from $\tilde{h}$ to $\tilde{h} + d\tilde{h}$ will be proportional to $n(\tilde{h})\tilde{h}^{2\gamma - 1}d\tilde{h}$, where $n(\tilde{h})$ is the number of features in the range. For this number density we assume another power law, namely, $n(\tilde{h}) = n_1(\tilde{h}/\tilde{h}_1)^{-\varepsilon}$. We introduce $n(\tilde{h})$ mainly to acknowledge that it need not be unity; the value of ε used in the examples to follow is only a guess. The reasons for the particular functional form are the same as for the relation (14), namely, monotonicity and integrability. Because of area averaging, the constants n_1 and h_1 will not appear in any results.

Since $\bar{V}$, $\bar{N}$ and $\bar{\rho}$ are assumed constant over the gridcell, we can use the stated assumptions about the mountain height distribution to integrate (13) with respect to area and obtain

$$
\begin{aligned}
\langle D_p \rangle &= a_0 \frac{H^<(2+\gamma-\varepsilon) + H^>(\gamma-\varepsilon-\beta)\tilde{h}_c^{2+\beta}}{H(2\gamma-\varepsilon)} \tilde{h}_0^{\gamma}(\bar{\rho}\bar{V}^3/\bar{N}L_0) \\
\langle D_{np} \rangle &= a_1 \frac{H^>(1+\gamma-\varepsilon) - H^>(\gamma-\varepsilon-\beta)\tilde{h}_c^{1+\beta}}{(1+\beta)H(2\gamma-\varepsilon)} \tilde{h}_0^{\gamma}(\bar{\rho}\bar{V}^3/\bar{N}L_0)
\end{aligned}
\qquad (15)
$$

for the average drag. Here $H(q) \equiv [(\tilde{h}_{max})^q - (\tilde{h}_{min})^q]/q$, and the superscript on H means that $\tilde{h}$ is replaced with either $\tilde{h}^< \equiv \min(\tilde{h}, \tilde{h}_c)$ or $\tilde{h}^> \equiv \max(\tilde{h}, \tilde{h}_c)$. The limit for small q is $H(0) = \log(\tilde{h}_{max}/\tilde{h}_{min})$. The integration over area is transformed to an integration over height bins, with limits h_{min} and h_{max}. The contribution from the partially blocked mountains in the numerator for D_p includes the effect of reducing the forcing area element dA by the factor $(\tilde{h}/\tilde{h}_c)^{-2\beta}$, as implied in Fig. 3. This kind of clipping from the sides is essentially the reverse of that described by Lindzen (1988) for the wavetrain itself.

The small-amplitude ($\tilde{h} \to 0$) limit of (15) is $\langle D \rangle \to D^*$, where

$$D^* \equiv a_0 \bar{\rho} \bar{N} \bar{V} \eta^2 / L_0 \tag{16}$$

and

$$\eta \equiv \frac{\bar{V}}{\bar{N}} \tilde{h}_0^{\gamma/2} \left[\frac{H(2+\gamma-\varepsilon)}{H(2\gamma-\varepsilon)} \right]^{1/2} . \tag{17}$$

As noted above, traditional schemes for linear base flux also use (16) but identify η with the root-mean-squared (RMS) height of the filtered topography. With η given by (17), D^* is proportional to $\langle h^{2-\gamma} \rangle$, instead of $\langle h^2 \rangle$, reflecting the covariance of L and h. The lower moment when $\gamma > 0$ yields a better universal match to the linear solution, as we show below. The ability to make the linear drag coefficient a weak function of latitude and longitude supports some of the foregoing assumptions and provides some confidence about the validity of the next step.

iii. Scaling of the analytical flux

From this point, the procedure to separate the base flux into linear and nonlinear parts is straightforward. We let a_0 be determined by $D^* = |\langle \tau \rangle|$ with D^* defined by (16) and $\langle \tau \rangle$ by (9). We use the result in (13), allowing (9) to determine the direction of the drag. As modified by the bulk dimensional analysis, the full base flux is then

$$\boxed{\langle \tau \rangle = \left(\frac{\langle D_p \rangle}{D^*} + \frac{\langle D_{np} \rangle}{D^*} \right) \tau^*,} \tag{18}$$

where τ now refers to the corrected drag, and τ^* to the original linear result (9). Only the nonlinear drag coefficient a_1 in the expression for D_{np} is undetermined. The nonpropagating part of (18) is available for forcing the resolved momentum below a reference level, while the propagating part is available for distribution over the column according to a level-by-level determination of wave saturation. Note that the propagating fraction cannot exceed unity but the sum of the two parts does not have this constraint.

Although the linear drag coefficient a_0 is no longer explicit, the strategy for choosing V

in the dimensional analysis should still be to minimize the variability of a_0 in time and space. The direction of τ^* varies between that of $-\bar{\boldsymbol{V}}$ in the case of isotropic terrain to that of the first eigenvector of $\mathbf{T}$ in the case of strongly anisotropic terrain. In the latter case, the drag is insensitive to the component of $\bar{V}$ in the direction of the *second* eigenvector, which is approximately orthogonal to the drag in that limit. Therefore, the tradition of taking V to be the component in the direction opposite the drag roughly optimizes the match between the dimensional and analytical drags with minimal variation in a_0. It also provides the physically relevant nondimensional mountain height, $\tilde{h} = Nh/V$, since Nh is the scale for the velocity perturbation in the drag direction for an individual mountain.

2c. Illustrative examples

In Fig. 4, we show the Northern Hemisphere distribution of linear base flux computed in three ways. The top panel displays the analytical drag (9) evaluated in the scalar form

$$D = \bar{V}\max(|T_1|, |T_2|), \tag{19}$$

where T_1 and T_2 are the eigenvalues of $\mathbf{T}$. The middle panel shows the traditional dimensional estimate using $\eta^2 = \langle h^2 \rangle$, the variance of the filtered topography. Finally, the bottom panel shows the new dimensional estimate, using (17) for η^2. In each case, we assume a uniform $\bar{V}$, $\bar{N}$ and $\bar{\rho}$, and normalize the result by the maximum drag, which occurs in the Himalayas. Both dimensional estimates fall short of the analytical drag almost everywhere outside the Himalayas, but the traditional estimate is quite a bit worse. The differences are most noticeable in Siberia and the central Rockies. Comparable discrepancies appear in the Andes and western Antarctica (not shown). As we have suggested, this is mainly because the dependence on h in (17) falls somewhere between the standard deviation and the mean topographic relief. The new result is based on $\gamma = 0.5$ and a constant L_0 (ε is irrelevant here for the reason mentioned just below). This choice for γ produces a slightly better match than the value, 0.4, suggested in the appendix.

For h_{min} and h_{max}, we did not use the actual minimum and maximum from the set of local extrema of high-pass topography within each cell. There is a great deal of scatter in the height distribution, as noted in the appendix. To produce a less erratic estimate of the height limits, we averaged the small-amplitude limit of D_p in (13) over the actual topographic data and equated the result to the small-amplitude limit of $\langle D_p \rangle$ in (15). This yielded the desired h_{max} after assuming $h_{min} = \mu h_{max}$ for some fixed μ. Fixing the ratio of h_{min} to h_{max} makes the *linear* drag estimate independent of ε. Since $h_{min} \ll h_{max}$ almost everywhere, the result is insensitive to μ for realistic choices. To integrate (13) over gridcells with bandpassed data, we took the integrand proportional to $h^{2-\gamma}$ and summed directly over area instead of bins. Integrating with respect to area fails to hold h and L fixed across individual mountains, but the consequence, based on our assumptions, is a constant multiplicative factor that depends on the mountain shape (β) and does not change the normalized drag estimate. We enforced $h > 0$ by subtracting the minimum value of all grid points within a bandpass radius (values had to be nudged to zero in the far field to avoid discontinuities). We enforced $h > 0$ in the same way to obtain the RMS result. Although this is not exactly the traditional RMS calculation, it is a slightly better match to the analytical drag and therefore shows the separate impact of γ. For the result in the Fig. 4 (bottom panel), we used $\mu = 0$.

The transition from linear flux to saturation flux for the two extreme cases of $\tilde{h}_{min}/\tilde{h}_{max}$ is shown in Fig. 5, in which $\langle D_p \rangle / D^*$ is graphed as a function of $\tilde{h}_{max}/\tilde{h}_c$ with $\gamma = 0.4$, $\beta = 0.5$ and $\varepsilon = 0$. Also shown is the total normalized drag $(\langle D_p \rangle + \langle D_{np} \rangle)/D^*$ based on the additional assumption that $a_1/a_0 = 9.0\tilde{h}_c$. This choice for a_1 produces a maximum total drag of approximately $2D^*$, which is a compromise between the maximum drags obtained in two- and three-dimensional nonlinear simulations, as summarized by Lott and Miller (1997) and Scinocca and McFarlane (2000). The broadest transitions in both D_p and D_{np} occur for $\tilde{h}_{min}/\tilde{h}_{max} \ll 1$. This broadening can be counteracted to some extent by increasing γ (not shown).

Shown in Fig. 6 is the bulk-dimensional drag for North and South America based on the same parameter choices as in Fig. 5. On the left is the total drag normalized by D^*, and on the right is the nonlinear fraction of the total drag. The large-scale wind, needed for determining the range of $\tilde{h}$, is taken to be purely zonal at 10 m/s everywhere. The critical mountain height is taken to be $\tilde{h}_c = 0.7$. This is a tuning choice that should depend on the procedure for determining h_{max}. Here we followed the method described just above, setting $h_{min} = 0$, and selected a critical mountain height that puts the high Andes near the maximum total drag (see Fig. 5). With this choice, we see that the flow over the Rocky Mountains is mostly linear, whereas the Himalayas (not shown) generate mostly nonlinear base flux.

3. Level-by-level determination of momentum forcing

To obtain the velocity tendency from $\partial\bar{V}/\partial t = \ldots - \bar{\rho}(z)^{-1} d\langle\tau\rangle/dz$, we need the vertical profile $\langle\tau(z)\rangle$. Let $\delta(z)$ denote the vertical particle displacement in a mountain wave [so that $\delta(0) = h$] and define $\tilde{\delta}(z) = \bar{N}\delta/\bar{V}$, where $\bar{N}(z)$ is the buoyancy frequency and $\bar{V}(z)$ is the resolved wind component in the direction opposite the net drag. Define $U(\tilde{\delta}, z) = \tilde{\delta} U_{sat}$, where $U_{sat}(z) = \sqrt{(\bar{\rho}/\rho_r)\bar{V}^3/\bar{N}L_0}$. Then $\rho_r U^2$ is proportional to the areally averaged pseudomomentum flux. The propagating part of the cell-averaged base flux (15) can now be expressed as

$$\boxed{\langle D_p\rangle = a_0 \frac{(2\gamma-\varepsilon)U_0^{\gamma}}{U_{max}^{2\gamma-\varepsilon} - U_{min}^{2\gamma-\varepsilon}} \rho_r [F_b + F_{ub}]\ ,} \tag{20}$$

where the contributions from the "broken" and "unbroken" parts of the field are, respectively,

$$
\begin{aligned}
F_b &= \frac{U_{max}^{\gamma'-\beta} - [U_c]^{\gamma'-\beta}}{\gamma'-\beta} U_c^{2+\beta} \\
F_{ub} &= \frac{[U_c]^{2+\gamma'} - U_{min}^{2+\gamma'}}{2+\gamma'} ,
\end{aligned}
\tag{21}
$$

with $[U_c] \equiv \min[U_{max}, \max(U_{min}, U_c)]$ and $\gamma' = \gamma - \varepsilon$. How will the drag change as a function of height as successive components attain $\delta = h_c$ and break?

The change to U in (20) is a z-dependent linear transformation of the original integration variable $\tilde{\delta}$. According to the theorem of Eliassen and Palm (1960), the value of U associated with a particular feature is independent of z until that part of the field breaks. The unbroken components are the only parts of the flux that depend on the amplitude of the source feature, or U. This allows us to fix the integration limits, U_{min} and U_{max}, and move all z-dependence in D_p to the saturation threshold U_c. The threshold is already z-dependent because the saturation value of $\tilde{\delta}$ depends on the minimum value of $h_c = (\bar{V}/\bar{N})\tilde{h}_c$ (dimensional) in the underlying column. We assume that the horizontal scale of an the individual feature does not change as a result of wavebreaking, so that U_0, associated with the constants in (14), is not a function of z. Therefore, the z-dependence in (20) is confined to F_b and F_{ub}.

Let $u_c(z) = \min|_{z' \le z}\{U_c(z')\}$. Then if the flux over each mountain is limited to the minimum of the saturation values, $D_c(z') \equiv \rho_r U_{sat}^2 \tilde{h}_c^2$, in the underlying column $z' < z$, the two parts of the flux $\langle D_p(z) \rangle$ are

$$
\boxed{
\begin{aligned}
F_b(z) &= \left(\frac{U_{max}^{\gamma'-\beta} - [u_c(0)]^{\gamma'-\beta}}{\gamma'-\beta} u_c(0)^{\beta} + \frac{[u_c(0)]^{\gamma'} - [u_c]^{\gamma'}}{\gamma'} \right) u_c^{\,2} \\
F_{ub}(z) &= \frac{[u_c]^{2+\gamma'} - U_{min}^{2+\gamma'}}{2+\gamma'} ,
\end{aligned}
}
\tag{22}
$$

where $[u_c] \equiv \min[U_{max}, \max(U_{min}, u_c)]$. The first contribution to F_b is due to components that are saturated at launch (hence the dependence on β), while the second is due to components that saturate above the ground. For the latter, we have assumed no further horizontal clipping. We have also assumed that the disturbance cannot gain energy from the environment or re-radiate any from breaking regions (*e.g.*, Bacmeister and Schoeberl, 1989). This means that, in layers where U_c increases with z, the residual flux from the broken components will hold constant at $\rho_r u_c^2 < D_c$, where $D_c \equiv \rho_r U_c^2$ is the local saturation value.

In Fig. 7, we graph $\langle D_p(z) \rangle / D^*$ to show the transition to saturation as a function of height above the mountains for two different ranges of h and an assumed environmental column described in the caption. The dotted curves show the momentum forcing, which is proportional to the derivative of $\langle D_p(z) \rangle$. Pseudomomentum is deposited in the layers where $\langle D_p \rangle$ is decreasing with height, which, in this example, occur near the ground and just above the two jets. The forced layers are broadened and full saturation is delayed when the terrain features within grid-cells vary most widely in height ($h_{min} = 0$).

4. Time-varying resolved flow

The steady problem is the limit in which advective time scales are much shorter than time scales of the background flow. If we simplify to a single background frequency, ω_0, and again denote with $\bar{V}_{\boldsymbol{k}}$ the resolved velocity projected onto the topographic wavenumber vector, the limit can be expressed as $\bar{V}_{\boldsymbol{k}} |\boldsymbol{k}| \gg |\omega_0|$. The opposite limit, $\bar{V}_{\boldsymbol{k}} |\boldsymbol{k}| \ll |\omega_0|$, is nearly as straightforward to analyze (Bell, 1975, gives the linear wave solution without these limiting assumptions). We show here that the resulting drag formula is almost the same as in the steady limit.

We obtain the total drag by integrating

$$\tau(x, y) = -p' \nabla \delta \tag{23}$$

along streamlines $\delta = h + \delta'$. The integral can be done after substituting the limiting solutions for the pressure perturbation p', and particle displacement, $\delta' \sim (\bar{V}_{\boldsymbol{k}}|\boldsymbol{k}|/|\omega_0|)h \to 0$. In the unsteady problem, the eddy momentum flux (7) and the form drag (23) are not interchangeable. In fact, the velocity components go out of phase and the vertical eddy momentum flux vanishes in the high-frequency limit with no background rotation.[1]

If $|\omega_0| \gg \bar{V}_{\boldsymbol{k}}|\boldsymbol{k}|$, we can proceed from (2) but using $m \approx -\bar{N}|\boldsymbol{k}|\,\mathrm{sgn}(\omega_0)/\sqrt{\omega_0^2 - f^2}$ for the vertical wavenumber. Here f is the Coriolis parameter, assumed slowly varying. Hydrostatic waves have been assumed by taking $|\omega_0| \ll \bar{N}$. Then (3) is replaced by

$$\partial(\bar{\rho}\hat{w})/\partial z = \bar{\rho}\left(-\frac{i\bar{N}|\boldsymbol{k}|}{\omega_0\alpha} - \frac{1}{2H}\right)i|\boldsymbol{k}|\bar{V}_{\boldsymbol{k}}\hat{h}, \tag{24}$$

where $\alpha \equiv \sqrt{1 - f^2/\omega_0^2}$. We still have that $\partial(\bar{\rho}w)/\partial z = -\nabla \cdot \bar{\rho}\boldsymbol{V}'$, and since the momentum equation implies

$$\left(\frac{\partial^2}{\partial t^2} + f^2\right)(-\nabla \cdot \bar{\rho}\boldsymbol{V}') = \frac{\partial}{\partial t}\nabla^2 p', \tag{25}$$

we may operate on (24) with the transform equivalent of $\nabla^{-2}\int dt(\partial^2/\partial t^2 + f^2)$ to reach

$$\hat{p} = \bar{\rho}\left(\frac{\bar{N}\alpha}{|\boldsymbol{k}|} - \frac{\alpha^2}{2H|\boldsymbol{k}|^2}i\omega_0\right)i|\boldsymbol{k}|\bar{V}_{\boldsymbol{k}}\hat{h}. \tag{26}$$

If $|\omega_0| > |f|$, the first term in (26) produces

$$p_0 = -\alpha\nabla\chi_0 \cdot \bar{\boldsymbol{V}}, \tag{27}$$

where χ_0 is defined by (5) or (6) (but in this case, $\nabla\chi_0$ is not the momentum perturbation). The correction for the mean density gradient, say $\hat{p}_1$, can be evaluated in terms of the field $A(x, y)$

[1] The high-frequency limit is determined by the terms $n = \pm 1$ in the solution by Bannon and Zehnder (1985), which includes a steady mean-flow component. Note, however, that their passing remark about the surface pressure in this limit is incorrect: the pressure perturbation does not vanish but is given by (26) below.

defined earlier. We find that

$$p_1 = \frac{\alpha^2}{2H}\bar{\rho}\frac{\partial \bar{\boldsymbol{V}}}{\partial t} \cdot \nabla A\,. \tag{28}$$

However, the perturbation is dominated by p_0 when $\lambda \ll H$. Since $|\omega_0| \ll \bar{N}$, this is the case if $|k|H \geq O(1)$.

We now put $\delta' = 0$ in (23) and substitute from (27) and (28) for the pressure. This yields

$$\tau = \alpha[\nabla\chi_0(\nabla h)^T]\bar{\boldsymbol{V}} + O(\lambda/H)\,, \tag{29}$$

which is the same as in the stationary case (8) except for the factor α and the different correction for mean density gradient. This result is directly relevant to internal waves generated by semidiurnal or higher-frequency tidal flows in the ocean (see Arbic *et al.*, 2004). It also applies to more general forcing with $|\omega| \gg |f|$ because the frequency dependence is weak in that limit.

Nonlinearity in the high-frequency limit is measured by the ratio $r = |\nabla \cdot \boldsymbol{V}'|/|\omega_0|$. This can be seen by writing the horizontal momentum advection as $(\nabla \cdot \boldsymbol{V}')\boldsymbol{V}' - \nabla \cdot \boldsymbol{V}'\boldsymbol{V}'$ and exploiting Gauss's Law and the far-field weakness of the horizontal flux. Then, from (24) and mass continuity, the nonlinearity is essentially

$$r \approx \frac{|\nabla^2 h|}{\alpha\omega_0^2}\bar{N}\bar{V}\,. \tag{30}$$

Projecting the velocity onto the alternating drag direction keeps $\bar{V}$ and r non-negative throughout the oscillation. Among other things, r is the ratio of the nonlinear to the linear dimensional drag estimates. Unlike the analogous parameter, $\tilde{h} \equiv \bar{N}h/\bar{V}$, for the steady problem, r depends on the horizontal scale L of the forcing, since $|\nabla^2 h| \sim h/L^2$. This will affect the nonlinear part of the base flux in the manner described next.

For the maximum or time-averaged linear drag, we have $D_l \sim \bar{\rho}\alpha\bar{N}\bar{V}h^2/L$ (reverting to the discrete meaning of *h*). The saturation drag D_{sat} is estimated by substituting for h in this expression, using (30) and $r = 1$. Thus, $D_{sat} \sim \bar{\rho}\alpha^3\omega_0^4L^3/\bar{N}\bar{V}$. In view of (30), we should normalize topographic height according to

$$\tilde{h} = \alpha^{-1}\left(\frac{\bar{V}}{\omega_0 L_0}\right)^2\frac{\bar{N}h}{\bar{V}}. \tag{31}$$

Then the horizontally averaged drag is calculated in the same way as (15), using the relations (12) and (14) for the horizontal scale. We find that

$$\begin{aligned}\langle D_p\rangle &= a_0\tilde{h}_0^{\gamma}\frac{H^<(2+\gamma-\varepsilon)+H^>(5\gamma-\varepsilon+3\beta)(\tilde{h}_0^{-4\gamma}\tilde{h}_c^{2-3\beta})}{H(2\gamma-\varepsilon)}(\bar{\rho}\alpha^3\omega_0^4L_0^3/\bar{N}\bar{V})\\ \langle D_{np}\rangle &= a_1\tilde{h}_0^{-3\gamma}\frac{H^>(1+5\gamma-\varepsilon)-H^>(5\gamma-\varepsilon-\beta)\tilde{h}_c^{1+\beta}}{(1+\beta)H(2\gamma-\varepsilon)}(\bar{\rho}\alpha^3\omega_0^4L_0^3/\bar{N}\bar{V})\,.\end{aligned} \tag{32}$$

Velocities are unbounded where $|\omega_0| = |f|$ because of resonance, but the pressure perturbation and the drag both vanish as these latitudes are approached from the equator (the saturation drag does so quite gradually). It follows from (31) that the drag becomes more and more linear (and D_{np} eventually drops out) as $\bar{V} \to 0$. Differences in the exponents compared to (15) are entirely due to the changed dependence on horizontal scale. The Eliassen-Palm constraint that underlies the traditional diagnosis of wavebreaking still applies to the maximum (or time-averaged) stress during the oscillation. The alterations to the vertical flux profile, given in the steady case by (20) and (22), are straightforward.

For the earth's semidiurnal tides, $\omega_0 \approx 1.4\times10^{-4}\ \mathrm{s}^{-1}$. Then, since the deep ocean tidal amplitude is $\bar{V} \approx 0.02\ \mathrm{ms}^{-1}$ (*e.g.*, Arbic *et al.*, 2004), the high-frequency limit is valid only at horizontal half-wavelengths, $\lambda_h = \pi/|\boldsymbol{k}|$, much greater than about 400 m. Near this transitional scale, (31) implies that h must be of order $\bar{V}/\bar{N}$, or about 100 m, in order to produce a nonlinear response (the factor α is irrelevant because the saturation drag is negligible near the resonant latitudes). At ten times the transitional scale, *i.e.*, at the scale of present-day global bathymetric datasets, h must be two orders of magnitude larger, or about 10 km, to produce a nonlinear response. Any nonlinearity in the high-frequency limit is thus confined to a narrow range of scales. Accordingly, most of the nonlinear drag on the semidiurnal tide is likely to occur at scales *shorter than* 400 m, where the disturbance should behave, at any tidal phase, as though the background flow were steady. In this range, the forcing would have to be extrapolated from the currently available topographic data and a semi-empirical relation like (14) might serve that purpose.

5. Summary

Linear analysis gives the vector drag due to stationary, hydrostatic, nonrotating internal waves forced by arbitrary topography. Therefore, statistical or dimensional characterizations of the subgrid terrain are not required for the *linear* base-flux computation at most of the relevant spatial scales. It turns out that the linear base-flux formula in the case of an unsteady resolved flow is virtually identical to that for a steady background flow in the limit $\omega \gg \bar{V}_{\boldsymbol{k}}|\boldsymbol{k}|$, where ω is the background frequency satisfying $\omega \ll \bar{N}$ and $\omega > |f|$.

The analytical drag due to stationary forcing can be made part of a practical closure for large-scale atmospheric models, while the analysis of the unsteady case can be used for parameterizing topographic drag due to semidiurnal tidal oscillations in the ocean. The correction for nonlinearity and the related formula for saturation flux continue to require an *ad-hoc* treatment. We have proposed a dimensional treatment of the nonlinearity that takes maximal advantage of the linear solutions. Dimensional analysis indicates that most of the nonlinearity in the semi-diurnal ocean tide is captured by the steady-state limit.

The base-flux scheme of Stern and Pierrehumbert (1988), to take one example, is essentially

$$D = G\frac{\tilde{h}^2}{a^2 + \tilde{h}^2}\rho V^3/NL, \tag{33}$$

in which G and a are fixed parameters. Analogous parameters are needed by more sophisticated schemes, including those of Baines and Palmer (1990), Lott and Miller (1997) and Scinocca and McFarlane (2000). The present approach eliminates the first of the two parameters (the linear drag coefficient) by providing the amplitude of the linear drag. It also provides the direction of the drag. The other parameter, a, is both the critical mountain height and part of the nonlinear drag coefficient, while the actual function chosen for the transition to nonlinearity is arbitrary. In the proposed scheme, the critical mountain height, $\tilde{h}_c$, and the nonlinear drag coefficient, a_1, remain free parameters. However, the functional form of the transition is less arbitrary because (15) incorporates information about the range of mountain heights within each gridcell, subject to an assumed power-law relation (14) between mountain height and width.

The present approach makes it possible to use raw statistics more sparingly than in previous schemes. The use of statistics has been reduced to a one-parameter height-width relation (14) needed to separate the nonpropagating drag from the propagating drag, and this is tightly constrained by the analytical solution. For base-flux estimates in *strongly* blocking regimes, we cannot yet say whether this approach improves on methods that are more dependent on statistical representations of the unresolved topography. However, our estimates of the propagating part are preferable to statistical approaches because the linear analysis extracts the most relevant information from the terrain data. The improvement almost certainly extends to mountains that are *marginally* blocking.

The sharpness of the transition to saturation determines the depth of the layers subjected to momentum forcing above the mountains. The forcing is therefore broadened by the proposed ensemble integration. Broadening due to non-parallel vertical shear and subgrid variation of drag orientation (Shutts 1995) was not considered here. We presume that there is no relationship between the subgrid drag orientation and subgrid mountain height, and consequently no simple correction of (21) for rotational shear. A possible solution is to introduce a probability distribution for drag angles analogous to (14). The ensemble integration would then be two-dimensional.

Appendix

Whether the relationship assumed in (14) is reasonable can be quickly judged from scatter plots of log-height versus log-width of actual terrain features. A naive approach to generating these values from the bandpassed data is as follows. A terrain "feature" is identified as any local maximum. Local minima are ignored because they would presumably share a width scale with a nearby maximum. Then $h > 0$ is enforced, as was done in the nonlinear drag analysis, by referring heights to the minimum value observed within the local bandpass radius. The widths are then estimated from the finite-difference Laplacian of the terrain height normalized by the height itself.

We find that the result of using the topographic data directly in this calculation is an essentially flat distribution of width that is dominated by the scale of the input grid. This is because the differences in the Laplacian operator strongly favor the smallest scales. To get a better picture of the mountain shape distribution, we instead carry out the above analysis on the velocity potential (6), which is a horizontal integral of height.

The plots in Fig. 8 focus on six geographical regions. The abscissa is the logarithm of normalized velocity potential χ, and the ordinate is the logarithm of the aforementioned function of velocity potential that can be interpreted as the width scale, namely the square-root of $A = -\chi/\nabla^2\chi$. The clustering of points near the mean is exaggerated by the filtering. Although the positive sign of the correlation is unambiguous, the scatter is considerable and difficult to distill. Correlation coefficients are just 0.2 to 0.3.

With this in mind, we have drawn, for each of the six regions, the principal component axis for a *subset* of the distribution formed by ignoring the largest scales. The justification for leaving out the largest scales is that the width computation at that end is strongly affected by interference from smaller features. When features are not cleanly separated, the distribution tends to becomes flat. The slopes of the principal component axes for the full distributions are generally 0.1 to 0.2, but when we exclude the mountains with dimension exceeding twice the mean (measured along the principal axis) we get the steeper slopes recorded in the plots. These range from about 0.3 to 0.5. Based on this analysis, we would settle on $\gamma = 0.4 \pm 0.1$ for the parameter in (14), with the largest values for the Andes and the Alps, and the smallest values for the Himalayas.

Acknowledgments

I am grateful to Brian Arbic for checking the analysis. I also benefited from discussions with Isaac Held, Jonas Nycander and John Scinocca about implementation and applicability. I thank Amy Braverman for some good advice on analyzing the scatter plots.

References

Arbic, B.K., S.T. Garner, R.W. Hallberg and H.L. Simmons, 2004: The accuracy of surface elevations in forward global barotropic and baroclinic tide models. *Deep-Sea Res. II*, **51**, 3069-3101.

Bacmeister, J.T., and M.R. Schoeberl, 1989: Breakdown of vertically propagating two-dimensional gravity waves forced by orography. *J. Atmos. Sci.*, **46**, 2109-2134.

Bacmeister, J.T., 1993: Mountain-wave drag in the stratosphere and mesosphere inferred from observed winds and a simple mountain-wave parameterization scheme. *J. Atmos. Sci.*, **50**, 377-399.

Baines, P.G., and T.N. Palmer, 1990: Rationale for a new physically based parametrization of subgridscale orographic effects. Tech. Memo. 169. European Centre for Medium-Range Weather Forecasts.

Bannon, P.R., and J.A. Zehnder, 1985: Surface pressure and mountain drag for transient airflow over a mountain ridge. *J. Atmos. Sci.*, **42**, 2454-2462.

Bell, T.H., 1975: Lee waves in stratified flows with simple harmonic time dependence. *J. Fluid Mech.*, **67-4**, pp. 705-722.

Eliassen, A., and E. Palm, 1960: On the transfer of energy in stationary mountain waves. *Geofysiske Publikasjoner*, **22**, 1-23.

Holton, J.R., 1973: An introduction to dynamical meteorology. Academic Press, New York, 361 pp.

Kim, Y.-J., and A. Arakawa, 1995: Improvement of orographic gravity wave parameterization using a mesoscale gravity wave model. *J. Atmos. Sci.*, **52**, 1875-1902.

Lindzen, R.S., 1981: Turbulence and stress due to gravity wave and tidal breakdown. *J. Geophys. Res,* **86**, 9707-9714.

Lindzen, R.S., 1988: Supersaturation of vertically propagating internal gravity waves. *J. Atmos. Sci.*, **45**, 705-711.

Lott, F., and M.J. Miller, 1997: A new subgrid-scale orographic drag parametrization: Its formulation and testing. *Quart. J. R. Meteor. Soc.*, **123**, 101-127.

Miranda, M.A., and I.N. James, 1992: Non-linear three-dimensional effects on gravity-wave drag: Splitting flow and breaking waves. *Quart. J. R. Meteor. Soc.*, **118**, 1057-1081.

Olaffson, H., and P. Bougeault, 1996: Nonlinear flow past an elliptic mountain ridge. *J. Atmos. Sci.*, **53**, 2465-2489.

Palmer, T.N., G.J. Shutts, and R. Swinbank, 1986: Alleviation of a systematic westerly bias in general circulation and numerical weather prediction models through an orographic gravity wave drag parameterization. *Quart. J. R. Meteor. Soc.*, **112**, 1001-1039.

Pierrehumbert, R.T, 1987: An essay on the parameterization of orographic gravity wave drag. *Proc. Seminar/Workshop on Observations, Theory and Modeling of Orographic Effects*,Vol. 1, Shinfield Park, Reading. UK, ECMWF, 251-282.

________________, and B. Wyman, 1985: Upstream effects of mesoscale mountains. *J. Atmos. Sci.*, **42**, 977-1003.

Scinocca, J.F., and N.A. McFarlane, 2000: The parametrization of drag induced by stratified flow over anisotropic orography. *Quart. J. R. Meteor. Soc.*, **126**, 2353-2393.

Shutts, G., 1995: Gravity-wave drag parametrization over complex terrain: The effect of critical-level absorption in directional wind-shear. *Quart. J. R. Meteor. Soc.*, **121**, 1005-1021.

Smith, R.B., 1977: The steepening of hydrostatic mountain waves. *J. Atmos. Sci.*, **34**, 1634-1654.

Stern, W.F., and R.T., Pierrehumbert, 1988: The impact of an orographic gravity-wave drag parameterization on extended range prediction with a GCM. Preprints, *Eighth Conf. on Numerical Weather Prediction*, Baltimore, MD. Amer. Meteor. Soc., 745-750.

Figure Captions

Fig. 1. The drag associated with stationary linear mountain waves over North and South America and western Antarctica. The arrow below the plot shows the scale for 2 Pa. The assumed surface wind is purely zonal at -7 m/s in the tropics and 13 m/s elsewhere. The assumed surface static stability and density are .01 s^{-1} and 1.0 kg/m^3, respectively. Averaging is over 1.5-deg square cells.

Fig. 2. The drag associated with stationary linear mountain waves over Asia. The scale for 2 Pa is shown by the arrow below the plot. The assumed surface wind is purely zonal at 10 m/s everywhere. The assumed surface static stability and density are as in Fig. 1. Averaging is over 1.5-deg square cells.

Fig. 3. Details of the scheme for separating the propagating part of the base flux from the nonpropagating (blocked or deflected) part. The hatched area is the cross-section presented to the blocked or deflected part of the flow.

Fig. 4. The distribution over the northern hemisphere of the linear drag computed in three ways: the analytical drag reduced to a scalar (top), the dimensional drag based on topographic variance (middle), and the dimensional drag based on (17) with $\gamma = 0.5$ (bottom). Values are normalized by the respective global maxima, which occur in the Himalayas. The output grid has a resolution of 2.0 deg in latitude by 2.5 degrees in longitude. The input grid is 1/30 deg in both directions.

Fig. 5. Normalized estimates, based on dimensional analysis, of the propagating drag, $\langle D_p \rangle / D^*$ (dashed), and total drag, $\langle D_p + D_{np} \rangle / D^*$ (solid), as a function of normalized maximum mountain height, h_{max}/h_c, for the two extreme cases $h_{min} = 0$ and $h_{min} = h_{max}$, with $\gamma = 0.4$, $\beta = 0.5$ and $\varepsilon = 0$. The drag is normalized by the linear estimate D^* defined by (16)

and (17). The nonpropagating part assumes $a_1 / a_0 = 9.0\tilde{h}_c$.

Fig. 6. The distribution over North and South America of the normalized total base flux (left) and non-propagating fraction (right) according to the bulk dimensional analysis, with $\gamma = 0.4$, $\beta = 0.5$ and $\varepsilon = 0$. The total base flux is normalized by $D^* + 0.05$, where D^* is the small-amplitude limit and the small increment (in units of Pa) serves to mask out regions of weak forcing. The output grid is the same as in Fig. 4. The assumed large-scale surface wind is zonal at $\bar{V} = 10$ m/s everywhere and the assumed static stability and density are as in Fig. 1. The critical mountain height is set to $\tilde{h}_c = 0.7$ to make the drag fully non-propagating (blocked) only in the highest parts of the Andes.

Fig. 7. The normalized pseudomomentum flux $\langle D_p(z) \rangle / D^*$ (solid) and normalized momentum forcing (dotted) as a function of height for the two extreme cases $h_{min} = 0$ and $h_{min} = h_{max}$, with $\gamma = 0.4$, $\beta = 0.5$, $\varepsilon = 0$ and $h_{max} = 1.2 h_c$. The assumed wind profile, shown at right, has jets of 38 m/s and 58 m/s centered at heights of 9 km and 25 km, respectively. The static stability increases from $0.011\ \mathrm{s}^{-1}$ to $0.022\ \mathrm{s}^{-1}$ across $z = 11$ km and the assumed density scale height is $H = 8$ km. The momentum forcing is normalized by D^* / H.

Fig. 8. Scatter plots of mountain “width” versus mountain “height” on log-log axes for six geographical regions. Width (ordinate) is estimated from the finite-difference Laplacian of the velocity potential, and height (abscissa) is identified with the velocity potential itself, referred to the local minimum value. Correlation coefficients range from 0.2 to 0.3. The line segments show the orientation of the principal components of the distributions excluding the largest features (see text), with the numerical slopes indicated at the bottom right of each plot.

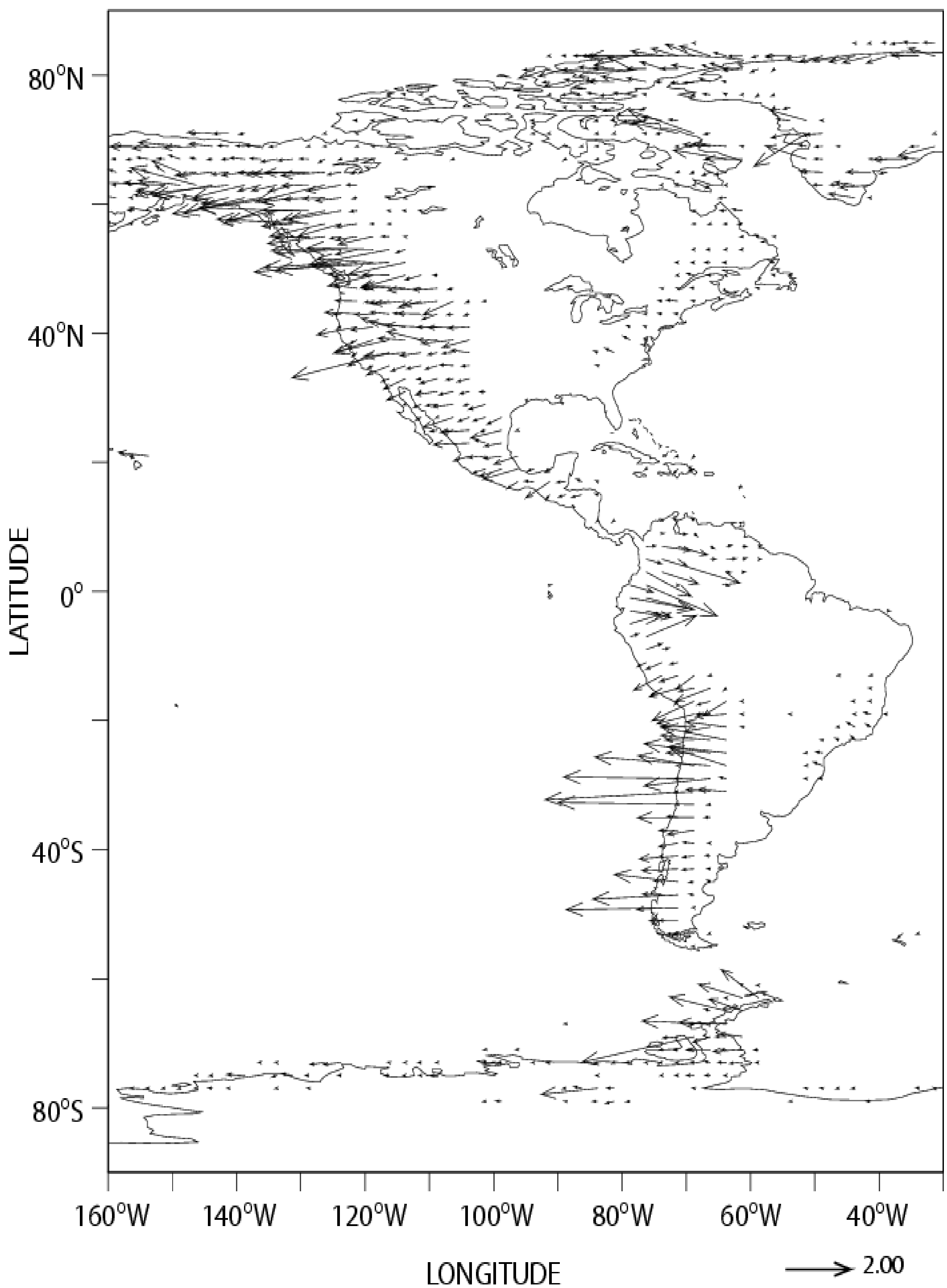

Fig 1. The drag associated with stationary linear mountain waves over North and South America and western Antarctica. The arrow below the plot shows the scale for 2 Pa. The assumed surface wind is purely zonal at -7 m/s in the tropics and 13 m/s elsewhere. The assumed surface static stability and density are .01 s^{-1} and 1.0 kg/m^3, respectively.

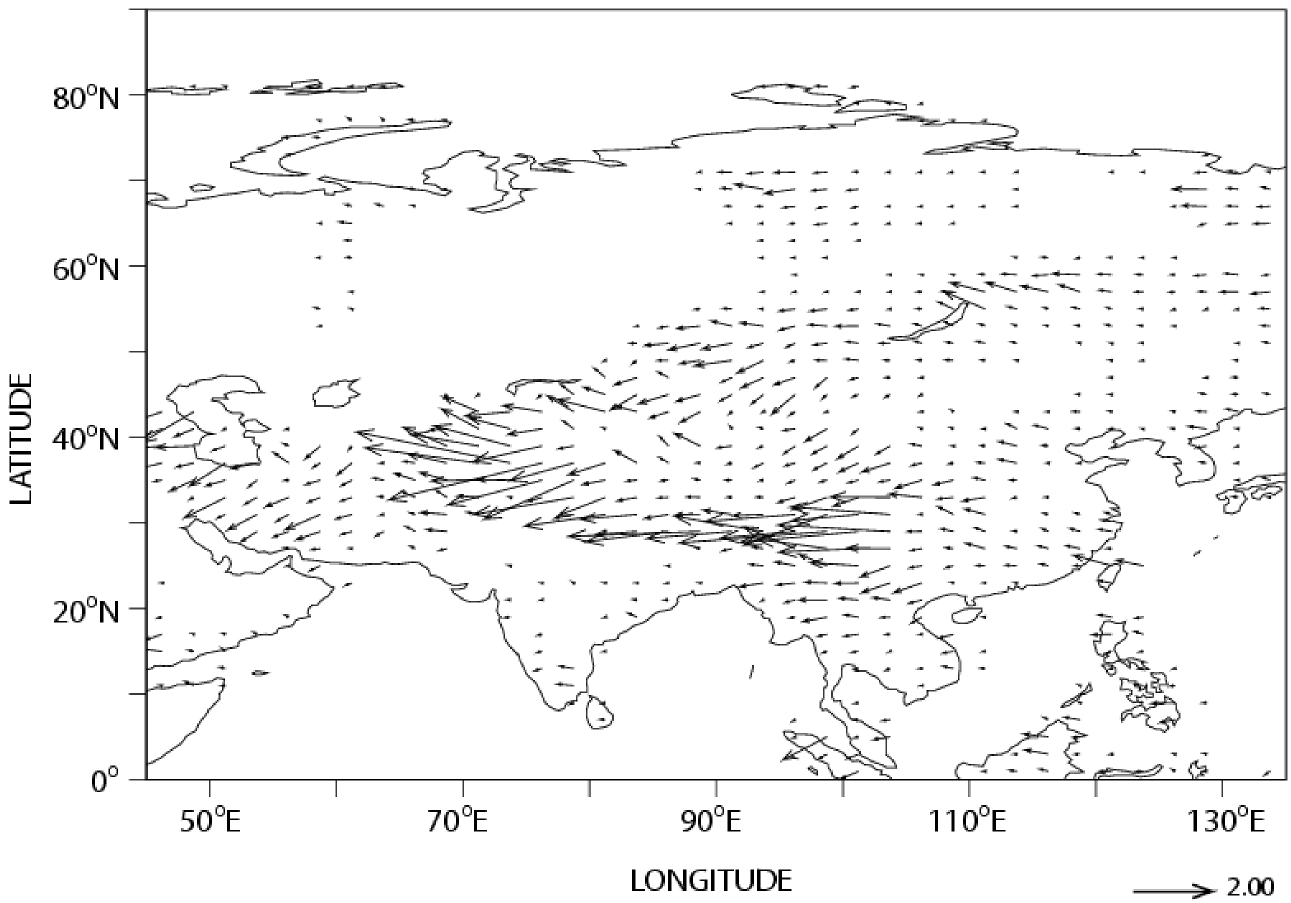

Fig 2. The drag associated with stationary linear mountain waves over Asia. The scale for 2 Pa is shown by the arrow below the plot. The assumed surface wind is purely zonal at 10 m/s everywhere. The assumed surface static stability and density are as in Fig. 1.

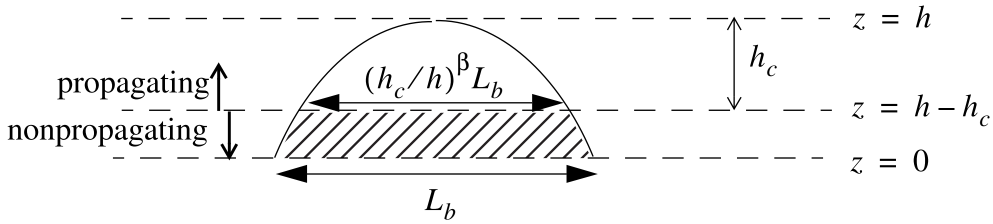

Fig. 3. Details of the scheme for separating the propagating part of the base flux from the non-propagating (blocked or deflected) part. The hatched area is the cross-section presented to the blocked or deflected part of the flow.

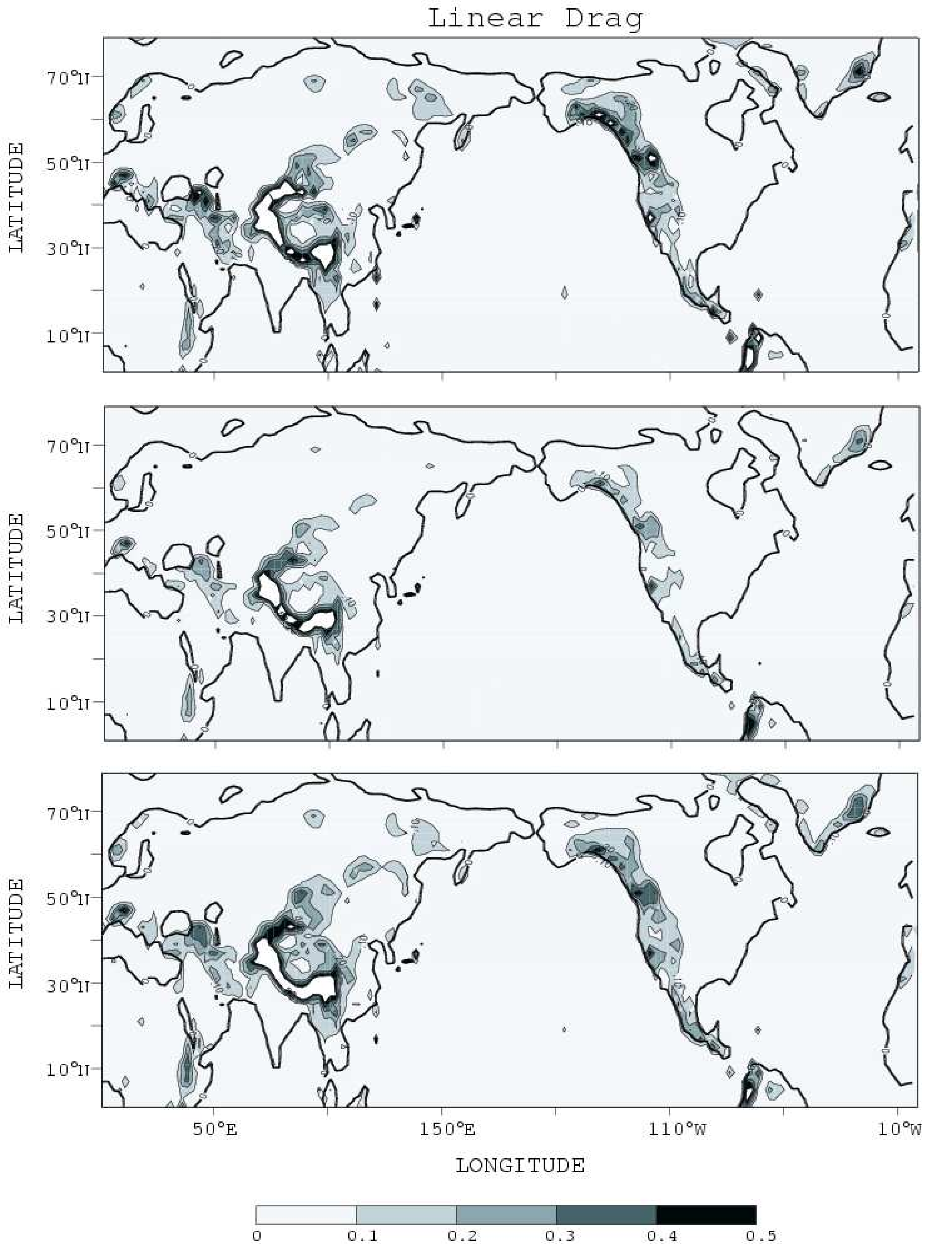

Fig. 4. The distribution over the northern hemisphere of the linear drag computed in 3 ways: the analytical drag reduced to a scalar (top), the dimensional drag based on topographic variance (middle), and the dimensional drag based on (17) with $\gamma = 0.5$ (bottom). Values are normalized by the respective global maxima, which occur in the Himalayas. The output grid has a resolution of 2.0 deg in latitude by 2.5 degrees in longitude. The input grid is 1/30 deg in both directions.

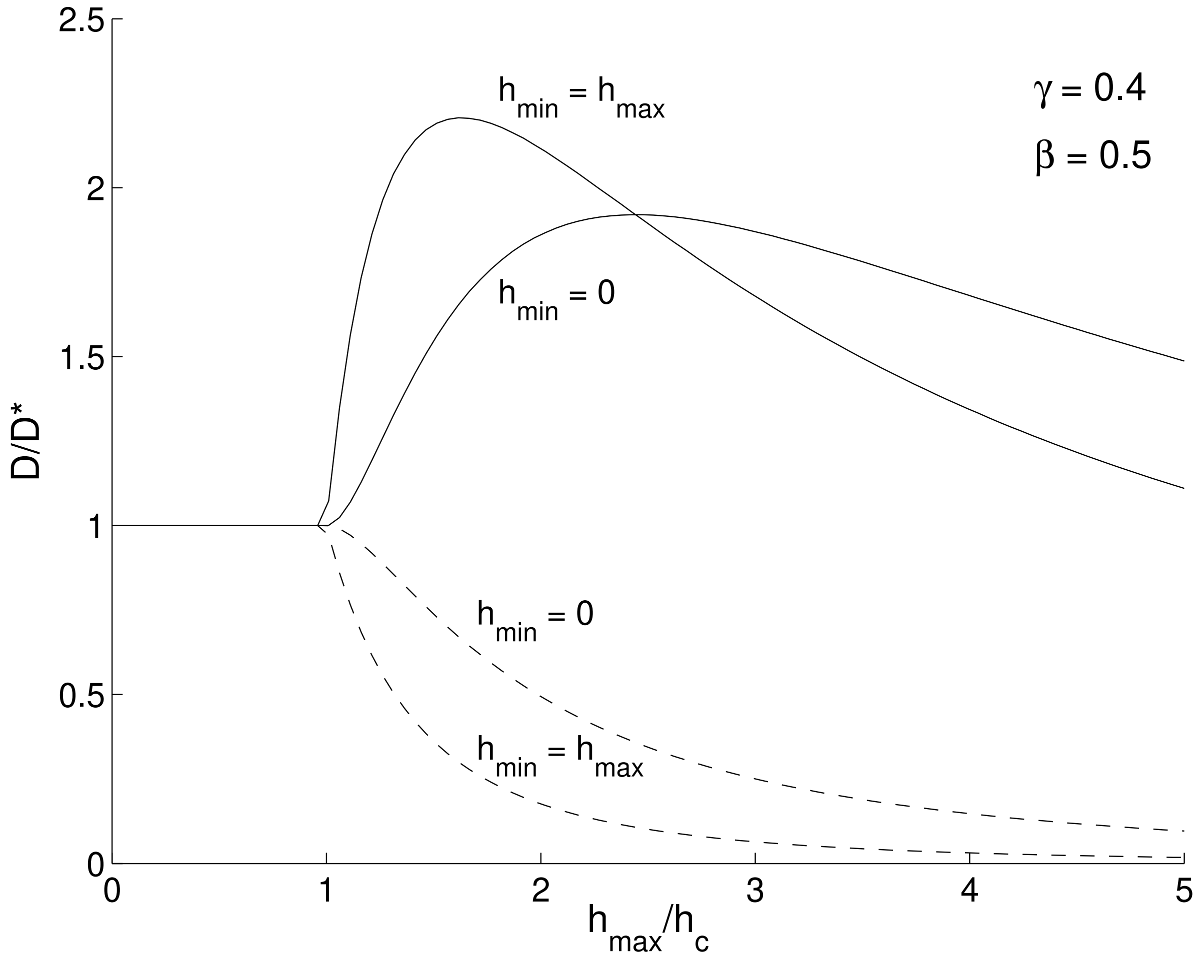

Fig. 5. Normalized estimates, based on dimensional analysis, of the propagating drag, $\langle D_p \rangle / D^*$ (dashed), and total drag, $\langle D_p + D_{np} \rangle / D^*$ (solid), as a function of normalized maximum mountain height, h_{max}/h_c, for the two extreme cases $h_{min} = 0$ and $h_{min} = h_{max}$ with $\gamma = 0.4$, $\beta = 0.5$ and $\varepsilon = 0$. The drag is normalized by the linear estimate D^* defined by (16) and (17). The nonpropagating part assumes $a_1 / a_0 = 9.0 \tilde{h}_c$.

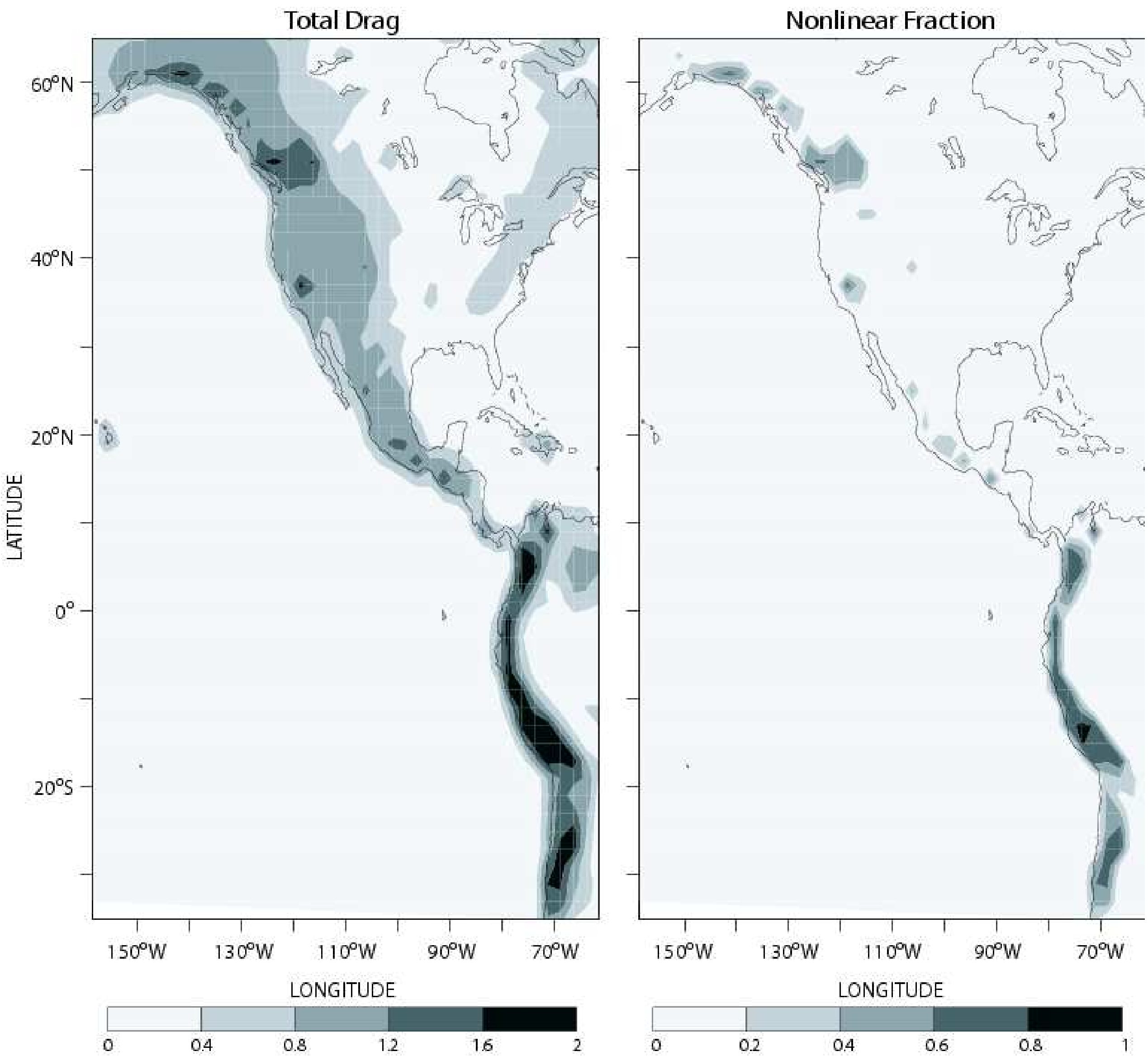

Fig. 6. The distribution over North and South America of the normalized total base flux (left) and non-propagating fraction (right) according to the bulk dimensional analysis, with $\gamma = 0.4$, $\beta = 0.5$ and $\varepsilon = 0$. The total base flux is normalized by $D* + 0.05$, where $D*$ is the small-amplitude limit and the small increment (in units of Pa) serves to mask out regions of weak forcing. The output grid is the same as in Fig. 4. The assumed large-scale surface wind is zonal at $\bar{V} = 10$ m/s everywhere and the assumed static stability and density are as in Fig. 1. The critical mountain height is set to $\tilde{h}_c = 0.7$ to make the drag fully non-propagating (blocked) only in the highest parts of the Andes.

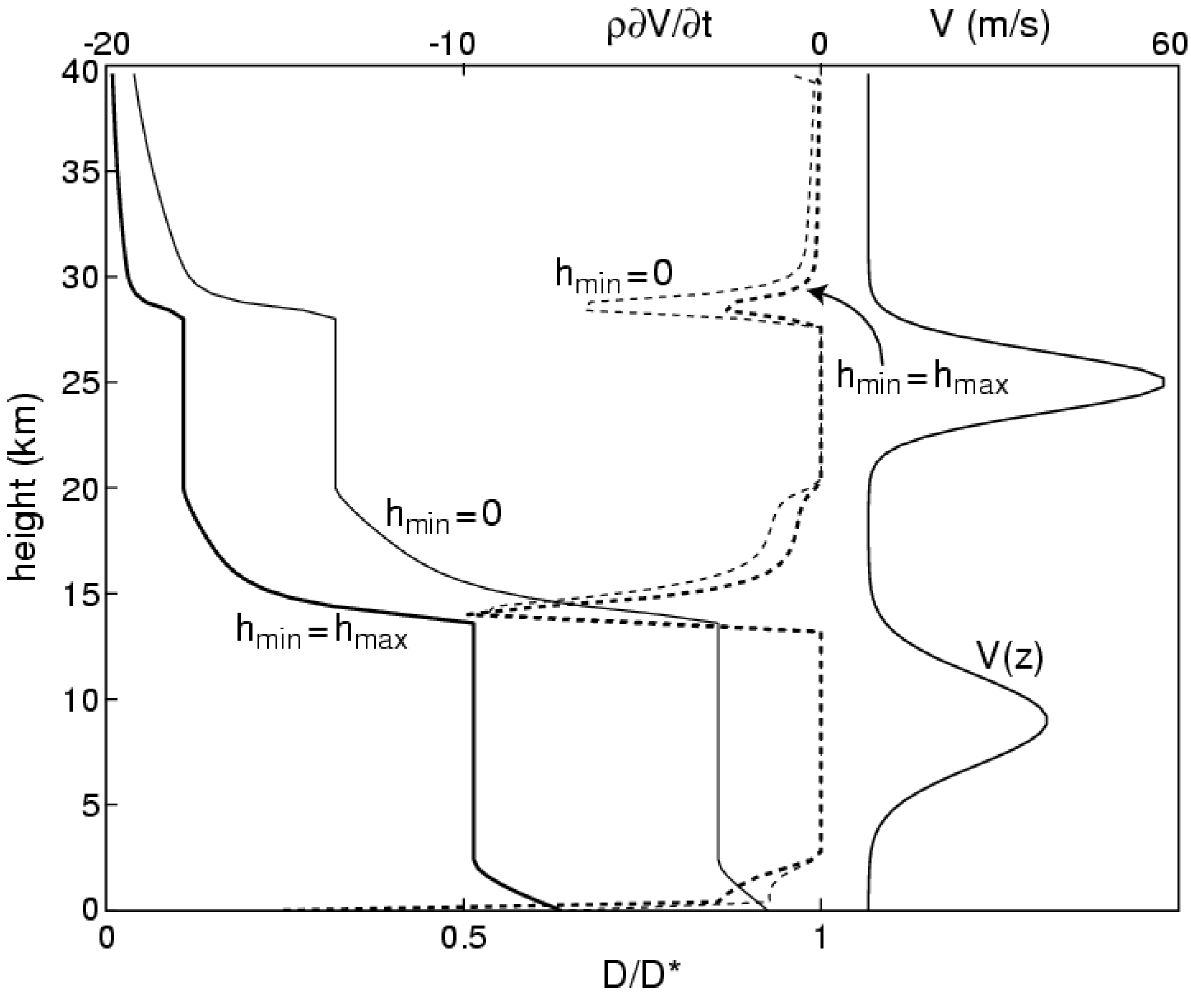

Fig. 7. The normalized pseudomomentum flux $\langle D_p(z)\rangle / D^*$ (solid) and normalized momentum forcing (dotted) as a function of height z for the two extreme cases $h_{min} = 0$ and $h_{min} = h_{max}$, with $\gamma = 0.4$, $\beta = 0.5$, $\varepsilon = 0$ and $h_{max} = 1.2 h_c$. The assumed wind profile, shown at right, has jets of 38 m/s and 58 m/s centered at heights of 9 km and 25 km, respectively. The static stability increases from $0.011\ \mathrm{s}^{-1}$ to $0.022\ \mathrm{s}^{-1}$ across $z = 11$ km and the assumed density scale height is $H = 8$ km. The momentum forcing is normalized by D^*/H.

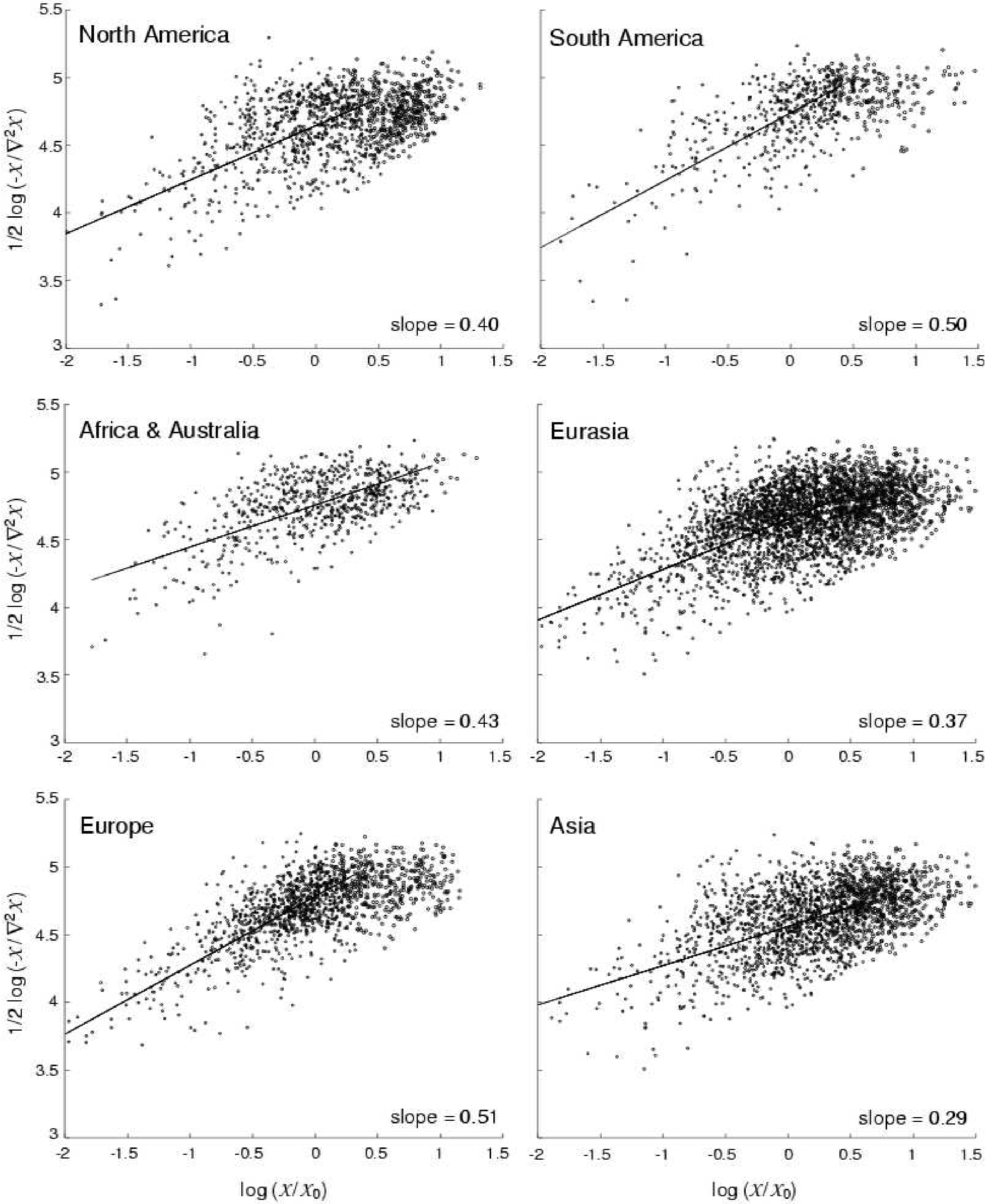
North America
slope = 0.40
South America
slope = 0.50
Africa & Australia
slope = 0.43
Eurasia
slope = 0.37
Europe
slope = 0.51
Asia
slope = 0.29
1/2 log (-$\mathcal{X}/\nabla^2\mathcal{X}$)
log ($\mathcal{X}/\mathcal{X}_0$)